RESEARCH ARTICLE

Check for updates

(C₁₃N₃H₁₄)₂MBr₄ (M = Zn, Cd): two novel hybrid metal halides with balanced integrated nonlinear optical performance†

Jiajing Wu,* Yi-Fan Fu, Wenlong Liu and Sheng-Ping Guo 🅾 *

The design and synthesis of high-performance nonlinear optical (NLO) crystals is a critical but intractable challenge in the development of advanced lasers technology. Herein, two novel zero-dimensional hybrid metal halides, namely, $(C_{13}N_3H_{14})_2ZnBr_4$ (**1**) and $(C_{13}N_3H_{14})_2CdBr_4$ (**2**), were successfully synthesized through a mild solution method. They crystalize in the orthorhombic noncentrosymmetric $Pna2_1$ space group. Both **1** and **2** exhibit good comprehensive NLO properties, including phase matchable and strong SHG effect (1.12× and 0.98 × KH_2PO_4), wide bandgaps (3.96 and 3.98 eV), large birefringences (0.15 and 0.12@1064 nm), and high laser-induced damage thresholds (28× and 25 × $AgGaS_2$), suggesting that they are promising NLO materials. In addition, the theoretical studies and crystal structure analysis reveal that their SHG responses and birefringences originate from the synergism of the ordered alignment of organic cations as well as the distorted $[MX_4]$ (M = Zn, Cd) tetrahedra. This work provides a new paradigm for designing and synthesizing high-performance NLO materials.

Introduction

Organic–inorganic hybrid metal halide perovskites have been identified as high-performance photovoltaic materials[1,2] and have demonstrated remarkable power conversion efficiency over the past decades. Other areas of optoelectronic applications such as solid-state lighting,[3] photodetectors,[4–6] sensors,[7] scintillators[8,9] and information encryption[10,11] have also been extensively studied. Meanwhile, the structural versatility, compositional tunability and unique physical properties of hybrid metal halides render them promising contenders for nonlinear optical (NLO) applications.[12,13]

NLO crystals that broaden the wavelength range of output radiation have attracted considerable attention in the fields of solid-state laser and NLO materials. Second-harmonic generation, (SHG) as one of the most fundamental NLO processes, has been widely used in a number of fields, including optical communication, medical treatment, laser technology, and sensor technology.[14,15] Generally, an optically desirable NLO crystal material should meet the following demanding conditions: (i) a non-centrosymmetric (NCS) structure is the prere-

quisite for NLO activity; (ii) a wide optical bandgap for obtaining high laser-induced damage thresholds (LIDTs); (iii) a significant SHG response at least larger than that of KH_2PO_4 (KDP); (iv) sufficient birefringence to achieve phase-matching (PM); (v) good physicochemical stability. Nevertheless, the integration of all the aforementioned superior properties into one structure remains a significant challenge.

Many methods have been proposed to obtain crystalline materials with NCS structures.[16–19] One common classic strategy involves the introduction of metal cations with stereo-chemically active lone-pair electrons (SCALP cation, *e.g.*, Bi^{3+}, Pb^{2+}, Ge^{2+}, *etc.*) or d^{10} metal cations (d^{10} cation, *e.g.*, Zn^{2+}, Cd^{2+}, Hg^{2+}, *etc.*). This strategy has been successfully employed for obtaining a variety of NLO crystals, such as $Sn_7Br_{10}S_2$,[20] $Rb_2SbC_2O_4Cl_3$,[21] $(PBA)_4BiI_7·H_2O$,[22] $MAGeBr_3$[23] and $Cs_3Pb_2(CH_3COO)_2X_5$ (X = I, Br).[24] Recent studies show that the SHG effect is not only associated with inorganic anionic units, but also with organic cations.[25] The introduction of chiral or asymmetric organic moieties (including π-conjugated/non-π-conjugated organic cations) has proven to be an effective strategy for obtaining SHG-active materials, and a series of novel hybrid metal halides with high SHG efficiencies, integrating the merits of both organic and inorganic moieties, were gained.[26] For example, Xu *et al.* synthesized NCS copper (I) halides with efficient SHG signal and high LIDT by using chiral ammonium cations.[27] Mao *et al.* synthesized a series of Ge-based bromide perovskites exhibiting tunable SHG response by adjusting the size of the organic cation, where

School of Chemistry and Chemical Engineering, Yangzhou University, Yangzhou, Jiangsu 225002, People's Republic of China. E-mail: jiajingw@yzu.edu.cn, spguo@yzu.edu.cn

7090 | *Inorg. Chem. Front.*, 2024, **11**, 7090–7097

This journal is © the Partner Organisations 2024

Inorganic Chemistry Frontiers   **Research Article**

Published on 05 zá 2024. Downloaded on 21.02.2026 17:44:02.

$(CH_3NH_3)GeBr_3$ shows a large SHG response (5 × KDP).[23] Our group recently synthesized two hybrid copper(I) halides NLO crystals by assembling an asymmetric organic molecule with a d^{10} metal cation.[28] OK group reported a Hg-based hybrid halides with a SHG effect of 5 × KDP and birefringence of 0.246 through incorporating π-conjugated melamine, d^{10} cation, and halide anion Cl^-.[29]

Combining the above strategies together, we put emphasis on the investigation of A–M^{II}–X (A = π-conjugated organic cations; M^{II} = d^{10} metal; X = Cl, Br, I) system and finally gained two new hybrid metal halides $(C_{13}N_3H_{14})_2ZnBr_4$ (**1**) and $(C_{13}N_3H_{14})_2CdBr_4$ (**2**). Their synthesis, structural chemistry, linear optical and NLO properties are comprehensively investigated in this study. Specifically, them both show PM SHG responses larger than that of KDP, wide bandgaps, large birefringences and high LIDTs, indicating their potential as promising NLO materials.

Experimental section

Materials

N,N-Diphenylguanidine monohydrobromide ($C_{13}H_{14}N_3Br$, 98%, Adamas), cadmium carbonate ($CdCO_3$, 99.99%, Adamas), zinc oxide (ZnO, 99.9%, Adamas), methanol (MeOH, AR, general reagent), hydrobromic acid (HBr, 40% in water, AR), and petroleum ether (AR, general reagent). They were used without further purification.

Syntheses

Single crystals of $(C_{13}H_{14}N_3)_2ZnBr_4$ (**1**) and $(C_{13}H_{14}N_3)_2CdBr_4$ (**2**) were synthesized by cooling crystallization method. Firstly, $C_{13}H_{14}N_3Br$ (1 mmol) was dissolved in 1 mL MeOH to form a clarified solution. Then, 0.5 mmol ZnO was dissolved in 300 μL HBr to form a colorless solution. Finally, the two solutions were thoroughly mixed in a 10 mL strain bottle. At 4 °C, colorless massive crystals were obtained after 24 h. The obtained crystals were washed with petroleum ether. The synthesis of **2** is similar to that of **1**, except that 300 μL HBr and 0.5 mmol ZnO were replaced by 200 μL HBr and 0.5 mmol $CdCO_3$.

Structure determination

At 296 K, single crystal data of **1** and **2** were acquired with a Bruker D8 QUEST X-ray diffractometer with Mo Kα radiation (λ = 0.71073 A). The structures of **1** and **2** were solved by Direct Methods, and the anisotropic displacement parameters of each atom were refined by full matrix least square F^2 method. Olex2 program[30] was used in all processes, and the structure was checked by PLATON program, and no key warning was found. Final improvements included anisotropic displacement parameters (ADP) and secondary extinction correction for all atoms. Crystallographic data, atomic coordinates and equivalent isotropic displacement parameters, bond lengths, bond angles, and hydrogen bonds are listed in Tables S1–S5.† CIF

documents were also deposited with CCDC numbers 2362939 (**1**) and 2362940 (**2**).†

Degree of tetrahedral distortion calculations

The magnitude of the asymmetric coordination environment of Zn^{2+} center in the $ZnBr_4$ tetrahedron can be evaluated using the following equations:[31]

$$\Delta d = \frac{1}{4}\sum_{i=1}^{4}\left[\frac{d_n - d_0}{d_0}\right]^2 \tag{1}$$

$$\delta^2 = \frac{1}{3}\sum_{i=1}^{4}(\theta_i - \theta_0)^2 \tag{2}$$

where d_n and d_0 represent the four individual M–Br bond lengths (Tables S3 and S4†) and the average M–Br bond length, respectively. θ_i represents the individual Br–M–Br bond angle of the tetrahedron and θ_0 is 109.5° in the regular tetrahedron.

Powder X-ray diffraction (PXRD)

The powder X-ray diffraction (PXRD) patterns were recorded by using a Bruker D8 Advance diffractometer with Cu-Kα radiation (λ = 1.5406 Å) operating at 40 kV and 100 mA. The simulated patterns were obtained by the Mercury program and single-crystal reflection data.

UV-vis-NIR diffuse reflectance spectrum

At room temperature, the absorption spectra of **1** and **2** were acquired with the Cary 5000 UV-Visible-near-infrared absorption spectrometer. Pure barium sulfate powder was used as the reference during collection. The experimental band gap value is obtained according to Tauc equation:[32]

$$(\alpha h\nu)^{1/n} = B(h\nu - E_g)$$

where α is the absorption coefficient, h is the Planck constant, ν is the frequency, B is a constant, E_g is the bandgap width of the semiconductor, and n is directly related to the type of semiconductor. When n = 1/2 for direct bandgap and n = 2 for indirect bandgap.

SHG measurements

Second-harmonic generation (SHG) measurements on powder crystalline samples of **1**, **2**, and benchmark KDP were carried out with the modified Kurtz-Perry method at 1064 nm laser.[33] The powder samples were sieved into six different ranges, including 25–75, 75–105, 105–150, 150–200, 200–250 and 250–315 μm, to measure their size-dependent SHG responses. The SHG signals were detected using photomultiplier tube and recorded *via* a digital oscilloscope.

Thermogravimetric analysis

Thermogravimetric analysis (TGA) were carried out on a TGA/DSC1 Mettler ToledoS6 thermal analyzer from 25 to 800 °C with a heating rate of 10 °C min^{-1} in the range of 25 to 800 °C under nitrogen.

This journal is © the Partner Organisations 2024   *Inorg. Chem. Front.*, 2024, **11**, 7090–7097 | **7091**

LIDT measurements

The single crystal' LIDTs of **1**, **2**, and AGS were measured using single-pulse measurement method by selecting flat surface crystals pressed into glass microscope cover slides. The samples were repeatedly irradiated by a 1064 nm laser with pulse width τ_p of 10 ns at a frequency of 1 Hz. Observations were made under an optical microscope and the laser power was increased until the damaged spots were observed. The laser power was then monitored and recorded with a Nova II sensor display with a PE50-DIT-C energy sensor, and the area of damage spots was measured as the damage threshold parameter of the sample. The damaged area was measured with a vernier caliper.

Theoretical calculations

The single-crystal structural data of **1** and **2** were used for theoretical calculations. The electronic structures and optical properties were calculated using a plane-wave basis set and pseudo-potentials within density functional theory (DFT) were implemented in the total-energy code CASTEP.[34] For the exchange and correlation functionals, Perdew-Burke-Ernzerh of (PBE) in the generalized gradient approximation (GGA) was chosen.[35] The interaction between the ionic cores and the electrons was described by the norm-conserving pseudopotential. The following valence-electron configurations were considered in the computation: $Zn\text{-}4s^24p^33d^{10}$, $Cd\text{-}5s^25p^24d^{10}$, $Br\text{-}4s^24p^5$, $C\text{-}2s^22p^2$, $N\text{-}2s^22p^3$, and $H\text{-}1s^1$. A plane-wave cutoff energy of 350 eV (**1**) and 310 eV (**2**), and $2 \times 2 \times 2$ (**1**, **2**) grid of Monkhorst–Pack points were employed for band structure and density of states calculations, which ensured good convergence of the computed structures and energies. The other parameters and convergence criteria were default values for the CASTEP code. The optical properties were calculated in terms of the real ($\varepsilon_1(\omega)$) and imaginary ($\varepsilon_2(\omega)$) parts of complex dielectric function $\varepsilon(\omega)$, $\varepsilon(\omega) = \varepsilon_1(\omega) + i\varepsilon_2(\omega)$.[36] The first-order nonresonant susceptibility of the low-frequency region is $x^1(\omega) = \varepsilon_1(\omega) - 1$, and the SHG tensors can be expressed in terms of the first-order susceptibilities as follows:[37]

$$\mathrm{X}_{ijk}^{(2)}(\omega_1,\omega_2,\omega_3) = \frac{ma}{N^2e^3}\mathrm{X}_{ii}^{(1)}(\omega_3)\mathrm{X}_{jj}^{(1)}(\omega_1)\mathrm{X}_{kk}^{(1)}(\omega_2) \qquad (3)$$

where m, N and e are the electron mass, atomic number density and electron charge respectively, parameter a ($a = \omega_0^2/d$, ω_0 and d are resonance frequency to each atom and lattice constant, respectively) characterizes the nonlinearity of the response, which can be obtained from experimental or theoretical estimations. The formula for calculating refractive index n is as follows:

$$n(\omega) = \frac{1}{\sqrt{2}}\left\{[\varepsilon_1(\omega)^2 + \varepsilon_2(\omega)^2]^{1/2} + \varepsilon_1(\omega)\right\}^{1/2} \qquad (4)$$

Results and discussion

Crystal structures

1 and **2** crystalize in the polar orthorhombic space group $Pna2_1$ (Tables S1–S5†). Since **1** and **2** are isostructural, the structure

of **1** will be described as the representation. As illustrated in Fig. 1, the fundamental building units in **1** are $ZnBr_4$ tetrahedron and $C_{13}N_3H_{14}^+$ organic cation, both of which are arranged along c direction, also the 2_1 helical axis direction (Fig. 1a and b). The organic cations and inorganic anions are connected by hydrogen bonds (Fig. S2†). Its structure is comprised of two crystallographically independent organic cations, exhibiting four distinct orientation arrangements (Fig. 1c). The polar $ZnBr_4$ tetrahedra form two types of layers (layer A and B) parallel with the bc plane, with the distance of 7.97 Å between the two layers. Because of the opposite orientation of $ZnBr_4$ tetrahedra within either layer A or B (Fig. 1d), the microscopic polarization in the ab plane is canceled out. Consequently, only the polarization along the c-axis is retained. The net dipole moments of inorganic units was calculated based on the bond-valence model,[38] the results are shown in Table S6 and Fig. S3.† The bond lengths of Zn–Br (2.3680(8) to 2.4729(8) Å) and the band angles of Br–Zn–Br (102.61° to 113.35°) in the $ZnBr_4$ tetrahedron greatly deviate from an ideal tetrahedron, indicating the $ZnBr_4$ tetrahedron exhibits high distortion. The distortion degree of $ZnBr_4$ and $CdBr_4$ tetrahedron are revealed by the distortion degree of bond length (Δd) and bond angle (δ^2), which are calculated to 2.52×10^{-4} and 22.78 for $ZnBr_4$ tetrahedron, respectively. For the $CdBr_4$ tetrahedron, the Δd and δ^2 are 2.68×10^{-4} and 51.27, respectively, slightly larger than those for $ZnBr_4$ tetrahedron (Table S7†). In addition, the experimental powder X-ray diffraction (PXRD) patterns of **1** and **2** are in accordance with the simulated ones, thereby confirming the obtained samples are pure (Fig. S4†).
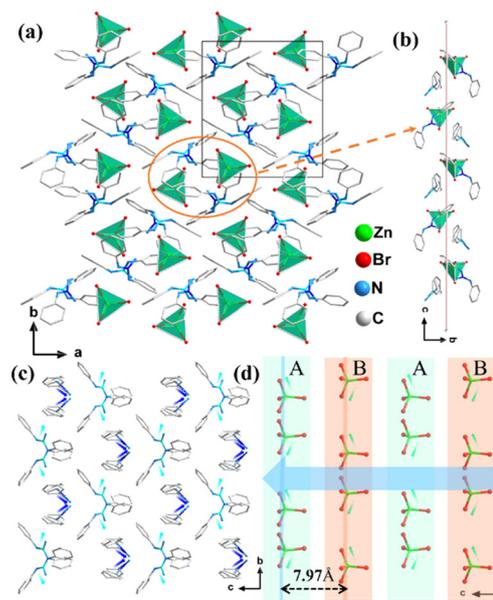

Fig. 1 (a) The structure of **1** along the c-axis; (b) the inorganic and organic parts rotating along the c axis with *pseudo*-2_1 helical arrangement; (c) the organic layers parallel with the ac plane; (d) the inorganic layers in the bc plane and their distance. Hydrogen atoms are omitted for clarity.

7092 | *Inorg. Chem. Front.*, 2024, **11**, 7090–7097

This journal is © the Partner Organisations 2024

Thermal analysis

To study the thermal properties of **1** and **2**, the thermogravimetric analysis (TGA) was measured under a nitrogen atmosphere, the results show that the initial decomposition temperatures of **1** and **2** are 285 °C and 282 °C, respectively, indicating good thermal stability (Fig. S5†).

Optical properties

The UV-vis absorption spectra of **1** and **2** in the range 200–600 nm are shown in Fig. 2(a and b). Their UV cutoff edges are 313 and 311 nm, corresponding to their bandgaps of 3.96 and 3.98 eV, respectively, consistent with their crystals' colors (Fig. S6†). Moreover, the bandgaps are comparable to many excellent NLO hybrid metal halides, such as $[C_5H_{12}N]$ $SnCl_3$ (3.40 eV),[39] $(TMA)_3Sb_2Cl_9$ (3.28 eV),[40] $(TpyH_3)(CdCl_4)Cl$ (2.85 eV),[41] $(PBA)_4InBr_7 \cdot H_2O$ (3.52 eV),[22] $(C_7H_{15}NCl)$ $SbCl_4$ (3.05 eV),[42] and $H_{11}C_4N_2CdI_3$ (3.86 eV).[43] Since both **1** and **2** crystallize with NCS structures, their powder SHG effects were investigated through the Kurtz-Perry method under 1.064 µm radiation with the benchmark KDP as reference. The particle size-dependent SHG data reveal that **1** and **2** exhibit type-I PM behavior (Fig. 2c and d), and their SHG responses are around 1.12 and 0.98 times that of KDP at the particle sizes of 250–315 µm, respectively, both of which are larger than those of most reported ionic metal halides containing d^{10} transition metal cations, the detailed data is shown in Table S8.† They are also larger than most reported ionic metal halides without d^{10} transition metal cations, such as $(C_4H_{10}NO)PbBr_3$ (0.81 × KDP),[44] $(Br-MM)_2MnBr_4$ (0.3 × KDP),[45] $(FEA)_3BiCl_6$ (0.6 × KDP),[46] $[BTMA]_2MnBr_4$ (0.59 × KDP),[47] and $(C_{10}H_{14}N)PbBr_3$ (1.05 × KDP).[48] In addition, as another important indicator for NLO materials, the LIDT was measured. The results display that the LIDTs of **1** and **2** are 226.01 and 199.14 MW cm^{-2}, much higher than that of AGS (7.97 MW cm^{-2}), suggesting that **1** and **2** have great potential for high-power NLO application.

Theoretical calculations

To further evaluate the SHG contribution units for **1** and **2**, the net dipole moments (DM) within a unit cell were calculated based on the point charge model.[49–51] It is assumed that the dipole moment centers of the positive charge for the $[C_{13}N_3H_{14}]^+$ cation and the negative charge for the $[MX_4]^{2-}$ anion are located at the C20 and M atoms, respectively. The average coordinates of C20 atom are (0.5, 0.5, 0.4281), and (0.5, 0.5, 0.3675) for Zn atom in **1** (Table S9, Fig. S7†). It is evident that the coordinates of positive and negative charges are not coincidence, thus producing DM. According to the equation $m = r \times q$, a DM (μ_{total}) of 20.47 D is obtained for **1**. Similarly, the calculated DM of **2** is 21.46 D (Table S9†). Because the SHG response is inversely correlated with the volume (Ω) and the square of the band gap (E_g^2). A corrected total DM (μ_c) was quantified using the following equation: $\mu_c = \mu_{total}/(\Omega \times E_g^2)$.[24,52] Consequently, the μ_c of **1** is 4.93×10^{-4} D (Å^3 eV^2)$^{-1}$, which is greater than 4.73×10^{-4} D (Å^3 eV^2)$^{-1}$ of **2**, in accordance with the experimental results.

In order to gain further insight into the relationship between structure and properties of **1** and **2** from the microscopic structural perspective, the first-principles calculations were implemented utilizing the PBE function. The band structures show that **1** and **2** are indirect band-gap compounds with theoretical band-gaps of 3.7 eV for **1** and 3.84 eV for **2** (Fig. 3a and b), which are agreement with the experimental results. Because the electronic structures of **1** and **2** are similar, only **1** was selected to illustrate the mechanism of the optical properties. The partial densities of states (PDOS) projected on each constitutional atom indicate that the Zn 3d, Br 4p, N 2p, C 2p, and H 1s states dominate the energy band ranging from −10 to 10 eV. The valence band maximum (VBM) of **1** is exclusively occupied by the Br 4p orbitals of the $[ZnX_4]^{2-}$ anion together with the C 2p and N 2p orbitals of the $(C_{13}N_3H_{14})^+$ cation. The conduction band minimum (CBM) of **1** is mainly occupied by the C 2p and N 2p orbitals of the $(C_{13}N_3H_{14})^+$ cation (Fig. 3c and d). **2** shows a similar trend. These results show that the band gaps and SHG properties of **1** and **2** are predominantly affected by the distortion of the [MX$_4$] tetrahe-
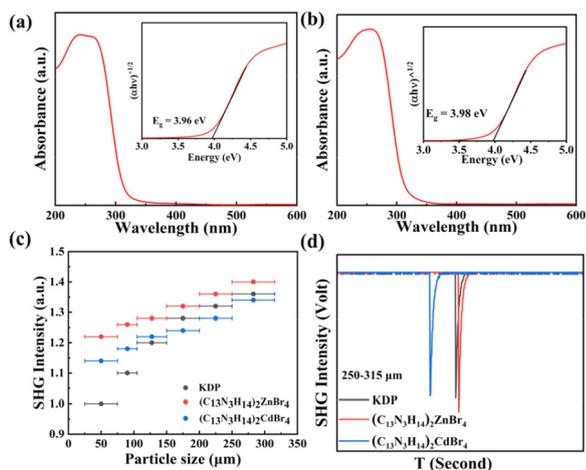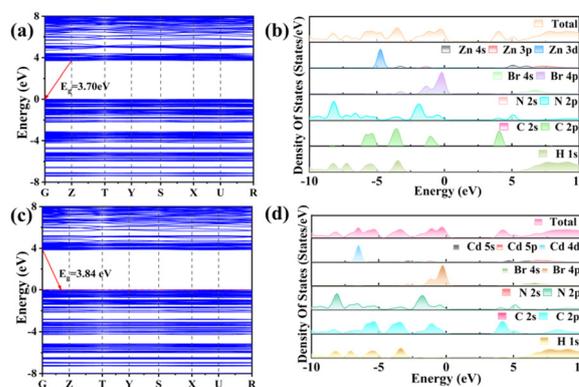

Fig. 2 UV-vis absorption spectra and the optical band gaps obtained from Tauc plots (inset) of (a) **1** and (b) **2**; (c) particle size-dependent SHG intensity of **1**, **2** and KDP at 1064 nm; (d) SHG intensity of **1**, **2** and KDP at particle sizes of 250−315 µm.

Fig. 3 Band structures of (a) **1** and (b) **2**; density of states of (c) **1** and (d) **2**. The Fermi level is set at 0 eV.

This journal is © the Partner Organisations 2024

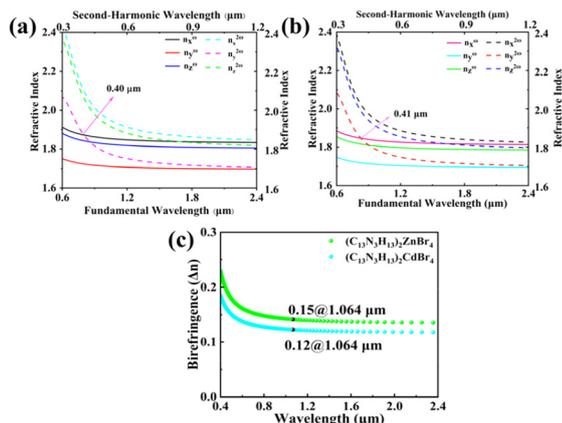*Inorg. Chem. Front.*, 2024, **11**, 7090–7097 | **7093**

Fig. 4 Calculated frequency-dependent NLO coefficients of (a) **1** and (b) **2**; calculated frequency-dependent refractive index and birefringences of (c) **1** and (d) **2**.

dra in the inorganic skeleton and the polar π-conjugated diphenyl guanidine organic cations $(C_{13}N_3H_{14})^+$.

As a result of the asymmetric space group $Pna2_1$ and Kleiman symmetry restriction, there are three nonvanishing independent NLO coefficients d_{15}, d_{24}, and d_{33} for **1** and **2** (Fig. S8†). The contribution to the three NLO coefficients of the constituent groups are summarized in Table S12.† The largest calculated d_{15} are 0.34 (**1**) and 0.32 (**2**) pm V^{-1}, corresponding to 0.87 and 0.82 times that of KDP (0.39 pm V^{-1}). Compared with the experimental value (1.12, 0.98 × KDP), it is slightly smaller. This difference can be ascribed to the reason that the theoretical values are based on periodic crystals,[53,54] while the experimental values are affected by the size and quality of the as-obtained crystals.

Both **1** and **2** crystallize in the orthogonal system, which belong to the dual axis crystal. The refractive index curve is exhibited in Fig. 4a and b, showing the trend of $n_x > n_z > n_y$. The shortest SHG phase-matching wavelength is 400 and 410 nm for **1** and **2**, respectively (Fig. 4a), confirming the PM capability of **1** and **2** under 1064 nm laser. The calculated birefringences $(\Delta n = n_x - n_y)$ is about 0.15@1064 and 0.12@1064 nm for **1** and **2**, respectively. Notably, the birefringence of **1** is larger than the reported hybrid metal halides such as (Morpholinium)$_2$Cd$_2$Cl$_6$ (0.0303@1064 nm),[55] [(CH$_3$)$_2$CH(CH$_2$)$_2$NH$_3$]$_2$(CH$_3$NH$_3$)$_2$Pb$_3$Cl$_{10}$ (0.02@546 nm),[56] (C$_{10}$H$_{11}$N$_3$)PbBr$_4$ (0.12@1064 nm),[57] (C$_9$H$_{14}$N)SbCl$_4$ (0.095@546 nm),[58] [(S)-3-aminopiperidine]PbI$_4$ (0.071@1064 nm),[59] and (C$_3$N$_6$H$_7$)$_3$HgCl$_5$ (0.093@1064 nm).[29] These results indicate that **1** and **2** exhibit good optical anisotropy, which they should be suitable potential candidates for NLO materials.

Conclusions

In conclusion, the two non-centrosymmetric hybrid metal halides, $(C_{13}N_3H_{14})_2MBr_4$, have been synthesized, which exhibit strong SHG effects, wide bandgaps, good optical an-

isotropy and large LIDTs. Additionally, first-principles calculations suggest that their optical properties are influenced synergistically by organic and inorganic components. This work not only enriches the family of hybrid metal halide NLO materials, but also provide an effective strategy for exploring potential NLO materials.

Author contributions

The manuscript was written through contributions of all authors. All authors have given approval to the final version of the manuscript.

Data availability

• The data supporting this article have been included as part of the ESI.†
• Crystallographic data for **1**–**2** has been deposited with the CCDC numbers of 2362939 and 2362940.†

Conflicts of interest

The authors declare that they have no conflict of interest.

Acknowledgements

References

1 J. J. Xue, R. Wang, X. H. Chen, C. L. Yao, X. Y. Jin, K. L. Wang, W. C. Huang, T. Y. Huang, Y. P. Zhao, Y. X. Zhai, D. Meng, S. Tan, R. Z. Liu, Z. K. Wang, C. H. Zhu, K. Zhu, M. C. Beard, Y. F. Yan and Y. Yang, Reconfiguring the Band-Edge States of Photovoltaic Perovskites by Conjugated Organic Cations, *Science*, 2021, **371**, 636–640.

2 J. J. Xue, R. Wang, K. L. Wang, Z. K. Wang, I. Yavuz, Y. Wang, Y. Yang, X. Gao, T. Huang, S. Nuryyeva, J. W. Lee, Y. Duan, L. S. Liao, R. Kaner and Y. Yang, Crystalline Liquid-Like Behavior: Surface-Induced Secondary Grain Growth of Photovoltaic Perovskite Thin Film, *J. Am. Chem. Soc.*, 2019, **141**, 13948–13953.

3 X. He, Q. Wei, H. Peng, Y. Li, X. Wang, B. Ke, J. Zhao and B. Zou, Large-Scale Room-Temperature Synthesis of the First Sb^{3+}-Doped Organic Ge(IV)-Based Metal Halides with Efficient Yellow Emission for Solid-State Lighting and

7094 | *Inorg. Chem. Front.*, 2024, **11**, 7090–7097

This journal is © the Partner Organisations 2024

Latent Fingerprint Detection, *Small Struct.*, 2024, **5**, 2300472.

4   Z. Li, Z. Deng, A. Johnston, J. Luo, H. Chen, Y. Dong, R. Sabatini and E. H. Sargent, Precursor Tailoring Enables Alkylammonium Tin Halide Perovskite Phosphors for Solid-State Lighting, *Adv. Funct. Mater.*, 2022, **32**, 2111346.

5   R. Li, Z. Wang, T. Zhu, H. Ye, J. Wu, X. Liu and J. Luo, Stereochemically Active Lone Pair Induced Polar Tri-layered Perovskite for Record-Performance Polarized Photodetection, *Angew. Chem., Int. Ed.*, 2023, **62**, e202308445.

6   L. Wang, C. Wu, Z. Xu, H. Wu, X. Dong, T. Chen, J. Liang, S. Chen, J. Luo and L. Li, Realization of High-Performance Self-Powered Polarized Photodetection with Large Temperature Window in a 2D Polar Perovskite, *Small*, 2023, **34**, 2110420.

7   L. Y. Yua, Y. Z. Shen, L. Chen, Q. Zhang, X. Y. Hu and Q. Xu, Molecularly Imprinted Ultrasensitive Cholesterol Photoelectrochemical Sensor Based on Perfluorinated Organics Functionalization and Hollow Carbon Spheres Anchored Organic-Inorganic Perovskite, *Biosens. Bioelectron.*, 2023, **237**, 115496.

8   K. Han, K. Sakhatskyi, J. Jin, Q. Zhang, M. V. Kovalenko and Z. Xia, Seed-Crystal-Induced Cold Sintering Toward Metal Halide Transparent Ceramic Scintillators, *Adv. Mater.*, 2022, **34**, 2110420.

9   P. Ran, L. Yang, T. Jiang, X. Xu, J. Hui, Y. Su, C. Kuang, X. Liu and Y. M. Yang, Multispectral Large-Panel X-ray Imaging Enabled by Stacked Metal Halide Scintillators, *Adv. Mater.*, 2022, **34**, 2205458.

10 H. Gong, H. Yu, Y. Zhang, L. Feng, Y. Tian, G. Cui and H. Fu, Thermally Activated Long Persistent Luminescence of Organic Inorganic Metal Halides, *Angew. Chem., Int. Ed.*, 2023, **62**, e202219085.

11 K. Liu, K. Liu, S. Hao, A. Hou, J. Cao, M. Quan, Y. Wang, C. Wolverton, J. Zhao and Q. Liu, Stimuli-Responsive Emission from Hybrid Metal Halides, *Adv. Funct. Mater.*, 2024, **34**, 2309296.

12 Q. Wang, J. Jin, Z. Wang, S. Ren, Q. Ye, Y. Dou, S. Liu, A. Morris, C. Slebodnick and L. Quan, Supramolecular Metal Halide Complexes for High-Temperature Nonlinear Optical Switches, *J. Am. Chem. Soc.*, 2024, **146**, 8971–8980.

13 Z. H. Guo, J. Z. Li, J. C. Liang, C. S. Wang, X. Zhu and T. C. He, Regulating Optical Activity and Anisotropic Second-Harmonic Generation in Zero-Dimensional Hybrid Copper Halides, *Nano Lett.*, 2022, **22**, 846–852.

14 M. Xin, P. Cheng, X. Han, R. Shi, Y. Zheng, J. Guan, H. Chen, C. Wang, Y. Liu, J. Xu and X. H. Bu, Resonant Second Harmonic Generation in Proline Hybrid Lead Halide Perovskites, *Adv. Opt. Mater.*, 2023, **11**, 2202700.

15 W. Huang, X. Zhang, Y. Li, Y. Zhou, X. Chen, X. Li, F. Wu, M. Hong, J. Luo and S. Zha, A Hybrid Halide Perovskite Birefringent Crystal, *Angew. Chem.*, 2022, **134**, e202202746.

16 X. Huang, S. H. Yang, X. H. Li, W. L. Liu and S. P. Guo, $Eu_2P_2S_6$: The First Ternary Rare-Earth Chalcophosphate Exhibiting Large Second-Harmonic Generation Response and High Laser-Induced Damage Threshold, *Angew. Chem., Int. Ed.*, 2022, **61**, e202206791.

17 X. Liu, W. L. Xu, S. R. Xu, X. Yu, Y. Q. Deng, X. H. Wu, F. Liang and Q. Wu, A Series of Organic-Inorganic Hybrid Compounds $[(C_2H_5)_4N]InCl_{4-x}Br_x$ (x = 0, 2, 4): Synthesis, Crystal Structure, and Nonlinear Optical Properties, *Inorg. Chem.*, 2020, **59**, 5721–5727.

18 W. F. Zhou and S. P. Guo, Rational Design of Novel Promising Infrared Nonlinear Optical Materials: Structural Chemistry and Balanced Performances, *Acc. Chem. Res.*, 2024, **57**, 648–660.

19 Y. Shang, J. Xu, H. Sha, Z. Wang, C. He, R. Su, X. Yang and X. Long, Nonlinear Optical Inorganic Sulfates: The Improvement of the Phase Matching Ability Driven by the Structural Modulation, *Coord. Chem. Rev.*, 2023, **494**, 215345.

20 X. H. Li, Z. H. Shi, M. Yang, W. L. Liu and S. P. Guo, $Sn_7Br_{10}S_2$: The First Ternary Halogen–Rich Chalco halide Exhibiting a Chiral Structure and Pronounced Nonlinear Optical Properties, *Angew. Chem.*, 2022, **134**, e202115871.

21 S. Han, A. Tudi, W. Zhang, X. Hou, Z. Yang and S. Pan, Recent Development of SnII, SbIII-based Birefringent Material: Crystal Chemistry and Investigation of Birefringence, *Angew. Chem., Int. Ed.*, 2023, **62**, e202302025.

22 D. Chen, S. Hao, L. Fan, Y. Guo, J. Yao, C. Wolverton, M. G. Kanatzidis, J. Zhao and Q. Liu, Broad Photoluminescence and Second-Harmonic Generation in the Noncentrosymmetric Organic-Inorganic Hybrid Halide $(C_6H_5(CH_2)_4NH_3)_4MX_7 \cdot H_2O$ (M = Bi, In, X = Br or I), *Chem. Mater.*, 2021, **33**, 8106–8111.

23 Y. Liu, Y.-P. Gong, S. Geng, M.-L. Feng, D. Manidaki, Z. Deng, C. C. Stoumpos, P. Canepa, Z. Xiao, W.-X. Zhang and L. Mao, Hybrid Germanium Bromide Perovskites with Tunable Second Harmonic Generation, *Angew. Chem., Int. Ed.*, 2022, **61**, e202208875.

24 Q. R. Shui, H. X. Tang, R. B. Fu, Y. B. Fang, Z. J. Ma and X. T. Wu, $Cs_3Pb_2(CH_3COO)_2X_5$ (X = I, Br): Halides with Strong Second–Harmonic Generation Response Induced by Acetate Groups, *Angew. Chem., Int. Ed.*, 2020, **60**, 2116–2119.

25 J. Cheng, G. Yi, Z. Zhang, Y. Long, L. Huang, H. Zeng, G. Zou and Z. Lin, In Situ Chiral Template Approach to Synthesize Homochiral Lead Iodides for Second-Harmonic Generation, *Angew. Chem., Int. Ed.*, 2023, **63**, e202318385.

26 J. J. Wu, Y. Guo, J. L. Qi, W. D. Yao, S. X. Yu, W. L. Liu and S. P. Guo, Multi–Stimuli Responsive Luminescence and Domino Phase Transition of Hybrid Copper Halides with Nonlinear Optical Switching Behavior, *Angew. Chem.*, 2023, **135**, e202301937.

27 F. Ge, B.-H. Li, P. X. Cheng, G. Li, Z. F. Ren, J. l. Xu and X.-H. Bu, Chiral Hybrid Copper(I) Halides for High Efficiency Second Harmonic Generation with a Broadband Transparency Window, *Angew. Chem., Int. Ed.*, 2022, **61**, e202115024.

28 J. L. Qi, J. J. Wu, Y. Guo, Z. P. Xu, W. L. Liu and S. P. Guo, Quasi-Linear CuX_2 (X = Cl, Br) Motif-Built Hybrid Copper

This journal is © the Partner Organisations 2024

Inorg. Chem. Front., 2024, **11**, 7090–7097 | **7095**

Halides Realizing Encouraging Nonlinear Optical Activities, *Inorg. Chem. Front.*, 2023, **10**, 3319–3325.

29 Z. Bai, J. Lee, H. Kim, C.-L. Hu and K. M. Ok, Unveiling the Superior Optical Properties of Novel Melamine-Based Nonlinear Optical Material with Strong Second-Harmonic Generation and Giant Optical Anisotropy, *Small*, 2023, **19**, 2301756.

30 O. V. Dolomanov, L. J. Bourhis, R. J. Gildea, J. A. K. Howard and H. Puschmann, H. OLEX,2: a Complete Structure Solution, Refinement and Analysis Program, *J. Appl. Crystallogr.*, 2009, **42**, 339–341.

31 K. Robinson, G. V. Gibbs and P. H. Ribbe, Quadratic Elongation: A Quantitative Measure of Distortion in Coordination Polyhedra, *Science*, 1971, **172**, 567–570.

32 Y. Guo, S. F. Yan, W. D. Yao, H. Y. Chen, W. L. Liu, J. J. Wu and S. P. Guo, Dual Monomeric Inorganic Units Constructed Bright Emissive Zero Dimensional Antimony Chlorides with Solvent-Induced Reversible Structural Transition, *Inorg. Chem.*, 2023, **62**, 13692–13697.

33 S. K. Kurtz and T. T. Perry, A Powder Technique for the Evaluation of Nonlinear Optical Materials, *J. Appl. Phys.*, 1968, **39**, 3798–3813.

34 M. D. Segall, P. L. D. Lindan, M. J. Probert, C. J. Pickard, P. J. Hasnip, S. J. Clark and M. C. Payne, First-Principles Simulation: Ideas, Illustrations and the CASTEP Code, *J. Phys.: Condens. Matter.*, 2002, **14**, 2717–2744.

35 J. P. Perdew, K. Burke and M. Ernzerhof, Generalized Gradient Approximation Made Simple, *Phys. Rev. Lett.*, 1996, **77**, 3865–38685.

36 S. F. Li, X. M. Jiang, B. W. Liu, D. Yan, C. S. Lin, H. Y. Zeng and G. C. Guo, Superpolyhedron-Built Second Harmonic Generation Materials Exhibit Large Mid-Infrared Conversion Efficiencies and High Laser-Induced Damage Thresholds, *Chem. Mater.*, 2017, **29**, 1796–1804.

37 X. M. Jiang, G. E. Wang, Z. F. Liu, M. J. Zhang and G. C. Guo, Large Mid-IR Second-Order Nonlinear-Optical Effects Designed by the Supramolecular Assembly of Different Bond Types without IR Absorption, *Inorg. Chem.*, 2013, **52**, 8865–8871.

38 I. D. Brown, Recent Developments in the Methods and Applications of the Bond Valence Model, *Chem. Rev.*, 2009, **109**, 6858–6919.

39 X. Liu, C. Ji, Z. Wu, L. Li, S. Han, Y. Wang, Z. Sun and J. Luo, [C$_5$H$_{12}$N]SnCl$_3$: A Tin Halide Organic-Inorganic Hybrid as an Above–Room–Temperature Solid–State Nonlinear Optical Switch, *Chem. – Eur. J.*, 2019, **25**, 2610–2615.

40 D. Chen, Z. Song, C. Yang, Y. Wei, G. Liu, L. Meng, Q. Wu and Y. Dang, Nonlinear Optical Effects of Hybrid Antimony (III) Halides Induced by Stereo active 5s^2 Lone Pairs and Trimethylammonium Cations, *Inorg. Chem.*, 2024, **63**, 10304–10311.

41 S. Wang, Z. Liang, X. Song, X. Huang, L. Liu, X. Jiang, Z. Lin and H. Liu, Photoluminescence and Nonlinear Optical Properties of Two Terpyridine-Based Hybrid Zn/Cd Halides, *Inorg. Chem.*, 2023, **62**, 21451–21460.

42 J.-M. Gong, T. Shao, P.-Z. Huang, C.-Y. Su, M. Chen, D.-W. Fu and H.-F. Lu, Reversible Phase Transition and Second-Harmonic Response Based on a Zero-Dimensional Organic-Inorganic Hybrid Compound, *J. Phys. Chem. C*, 2022, **126**, 15274–15279.

43 H. Y. Wu, C. L. Hu, M. B. Xu, Q. Q. Chen, N. Ma, X. Y. Huang, K. Z. Du and J. Chen, From H$_{12}$C$_4$N$_2$CdI$_4$ to H$_{11}$C$_4$N$_2$CdI$_3$: a Highly Polarizable CdNI$_3$ Tetrahedron Induced a Sharp Enhancement of Second Harmonic Generation Response and Birefringence, *Chem. Sci.*, 2023, **14**, 9533–9542.

44 C. Shen, D. Sun, Y. Dang, K. Wu, T. Xu, R. Hou, H. Chen, J. Wang and D. Wang, (C$_4$H$_{10}$NO)PbX$_3$ (X = Cl, Br): Design of Two Lead Halide Perovskite Crystals with Moderate Nonlinear Optical Properties, *Inorg. Chem.*, 2022, **61**, 16936–16943.

45 Y. Wang, T. Zhang, M.-M. Lun, F.-L. Zhou, D.-W. Fu and Y. Zhang, Halogen Regulation Triggers NLO and Dielectric Dual Switches in Hybrid Compounds with Green Fluorescence, *Inorg. Chem. Front.*, 2021, **8**, 4230–4238.

46 L.-L. Chu, T. Zhang, Y.-F. Gao, W.-Y. Zhang, P.-P. Shi, Q. Ye and D.-W. Fu, Fluorine Substitution in Ethylamine Triggers Second Harmonic Generation in Noncentrosymmetric Crystalline [NH$_3$CH$_2$CH$_2$F]$_3$BiCl$_6$, *Chem. Mater.*, 2020, **32**, 6968–6974.

47 Y. Guo, J. J. Wu, W. L. Liu and S. P. Guo, Organic Cation Modulation Triggered Second Harmonic Response in Manganese Halides with Bright Fluorescence, *Inorg. Chem.*, 2022, **61**, 11514–11518.

48 K. Li, H. Ye, X. Li, X. Wang, J. Luo and X. Liu, Rational Design of an Organic-Inorganic Hybrid with Schiff Base Cations for an Efficient Quadratic Nonlinear Optical Switch, *Inorg. Chem. Front.*, 2022, **10**, 435–442.

49 Y. Zhang, W. Q. Liao, D. W. Fu, H. Y. Ye, Z. N. Chen and R. G. Xiong, Highly Efficient Red-Light Emission in An Organic-Inorganic Hybrid Ferroelectric: (Pyrrolidinium) MnCl$_3$, *J. Am. Chem. Soc.*, 2015, **137**, 4928–4931.

50 Z. H. Sun, J. H. Luo, S. Q. Zhang, C. M. Ji, L. Zhou, S. H. Li, F. Deng and M. C. Hong, Solid-State Reversible Quadratic Nonlinear Optical Molecular Switch with an Exceptionally Large Contrast, *Adv. Mater.*, 2013, **25**, 4159–4163.

51 S. S. Wang, Y. P. Yao, J. T. Kong, S. G. Zhao, Z. H. Sun, Z. Y. Wu, L. N. Li and J. H. Luo, Highly Efficient White-Light Emission in a Polar Two-Dimensional Hybrid Perovskite, *Chem. Commun.*, 2018, **54**, 4053–4056.

52 Z. Ma, J. Hu, R. Sa, Q. Li, Y. Zhang and K. Wu, Screening Novel Candidates for Mid-IR Nonlinear Optical Materials from I$_3$−V−VI$_4$ Compounds, *J. Mater. Chem. C*, 2017, **5**, 1963–1972.

53 M. L. Liang, Y. X. Ma, C. L. Hu, F. Kong and J. G. Mao, Ba (MoO$_2$F)$_2$(QO$_3$)$_2$ (Q = Se, Te): Partial Fluorination of MoO$_6$ Octahedra Enabling Two Polar Solids with Strong and Phase Matchable SHG Response, *Chem. Mater.*, 2020, **32**, 9688–9695.

54 R. L. Tang, M. Yan, W. D. Yao, W. L. Liu and S. P. Guo, HgTeO$_2$F(OH): A Nonlinear Optical Oxyfluoride Constructed

7096 | *Inorg. Chem. Front.*, 2024, **11**, 7090–7097

This journal is © the Partner Organisations 2024

of Active $[TeO_2F(OH)]^{2-}$ Pyramids and V-Shaped $[HgO_2]^{2-}$ Groups, *Inorg. Chem.*, 2022, **61**, 2333–2339.

55 D. F. Sun, D. l. Wang, Y. Y. Dang, S. B. Zhang, H. Z. Chen, R. X. Hou, K. Wu and C. Y. Shen, Organic-Inorganic Hybrid Noncentrosymmetric (Morpholinium)$_2$Cd$_2$Cl$_6$ Single Crystals: Synthesis, Nonlinear Optical Properties, and Stability, *Inorg. Chem.*, 2022, **61**, 8076–8082.

56 W. J. Qi, M. Yu, W. Z. Jian, L. X. Tao, H. S. Guo, L. Yi, G. W. Qian, L. J. Hua and S. Z. Hua, Unusual Ferroelectric-Dependent Birefringence in 2D Trilayered Perovskite-Type Ferroelectric Exploited by Dimensional Tailoring, *Matter*, 2021, **5**, 194–205.

57 L. L. Zhang, Q. R. Ding, P. H. Wang, Y. Q. Zhang, Q. Y. Liu, Y. L. Wang and J. H. Luo, Achieving Strong Second Harmonic Generation Effects Induced Via Dimensional Increase of PbX$_6$ Octahedra and Halogen Substitutes in (C$_{10}$H$_{11}$N$_3$)PbX$_4$ (X = Cl or Br), *Inorg. Chem. Front.*, 2024, **11**, 3618–3625.

58 F. F. Wu, Q. Y. Wei, X. Q. Li, Y. Liu, W. Q. Huang, Q. Chen, B. X. Li, J. H. Luo and X. T. Liu, Cooperative Enhancement of Second Harmonic Generation in an Organic-Inorganic Hybrid Antimony Halide, *Cryst. Growth Des.*, 2022, **22**, 3875–3881.

59 D. Fu, J. Xin, Y. He, S. Wu, X. Zhang, X. M. Zhang and J. Luo, Chirality-Dependent Second-Order Nonlinear Optical Effect in 1D Organic-Inorganic Hybrid Perovskite Bulk Single Crystal, *Angew. Chem., Int. Ed.*, 2021, **60**, 20021–20026.

This journal is © the Partner Organisations 2024

Inorg. Chem. Front., 2024, **11**, 7090–7097 | **7097**